Co-modulated interface binding energy and electric field distribution of layer-structured PVDF–LDPE dielectric composites with $BaTiO_3$: experiment and multiscale simulations

Ruitian Bo[1], Chunfeng Wang[1], Yongliang Wang[1], Peigang He[2], and Zhidong Han (✉)[1,3]

1 School of Materials Science and Chemical Engineering, Harbin University of Science and Technology, Harbin 150040, China
2 School of Materials Science and Engineering, Harbin Institute of Technology, Harbin 150001, China
3 Key Laboratory of Engineering Dielectrics and Its Application (Ministry of Education), Harbin University of Science and Technology, Harbin 150080, China

E-mail: zhidong.han@hrbust.edu.cn

Supplementary material

1 Experimental compositions of the composites

Melt blending method was used to prepare LDPE- or PVDF-based composites according to the compositions in Table S1. The layer-structured composites were then prepared by mold pressing with the sheets of LDPE- or PVDF-based composites.

Table S1 Compositions of LDPE- or PVDF-based composites

Sample	LDPE-based composites		PVDF-based composites	
	V(LDPE)/vol.%	*V*(BT)/vol.%	*V*(PVDF)/vol.%	*V*(BT)/vol.%
LDPE	100	–	–	–
BT20/LDPE	80	20	–	–
PVDF	–	–	100	–
BT20/PVDF	–	–	80	20
PVDF–LDPE	100	–	100	–
PVDF–BT20/LDPE	80	20	100	–
BT20/PVDF–LDPE	100	–	80	20
BT20/PVDF–BT20/LDPE	80	20	80	20

According to the study by Wang et al. [1], the layer-structured composite with 20 vol.% BT showed high breakdown field strength and energy density while maintaining a large dielectric permittivity and a low dielectric loss. This paper refers to the research results of Wang et al. and adopts the BT content of 20 vol.% in order to investigate the influences of layered structure on the dielectric properties of the composites while achieving a high dielectric permittivity and improving the breakdown field strength.

2 Details of the MD simulation

The geometric structure was optimized through the Smart algorithm on the initial model, the energy convergence level was set to 0.0001 kcal·mol^{-1}, and the force convergence level was set to 0.005 kcal·mol^{-1}·Å^{-1}, and then MD simulation was performed. Firstly, the model system was annealed. The system was heated from 298.0 to 500.0 K at 40.4 K intervals, and then cooled back to 298.0 K at 40.4 K intervals. The annealing cycle was performed 5 times in the NVT ensemble for a total of 1000 ps MD simulation. Secondly, a 500 ps MD simulation was performed in the NPT ensemble under the conditions of 298 K and 1 standard atmospheric pressure. The temperature control method was Nose [2], the pressure control method was Berendsen [3], and the force field was universal force field (UFF) [4–5]. van der Waals and electrostatic forces were calculated with the cut-off radius of 15.5 Å by atom-based method and Ewald method, respectively. Finally, the NPT dynamic trajectory of 500 ps was used for calculation and structural analysis.

The rationality of the initial models was evaluated according to the simulation results of the density [6–7]. As an example, the density of LDPE and BT20/LDPE was simulated to verify the rationality and practicability of the models. The simulated density was obtained and compared with the measured density in Table S2. The simulated results showed good consistency with the measured results, which evidenced the good feasibility of the models.

Table S2 The densities of LDPE and BT20/LDPE

Sample	Simulated density/(g·cm^{-3})	Measured density/(g·cm^{-3})
LDPE	0.87	0.90
BT20/LDPE	1.70	1.80

During MD simulations, the system was expected to achieve a statistical equilibrium in order to ensure the accuracy of the simulated results [8–9]. Generally, the fluctuation range of energy and temperature curve is controlled within 5%–10%, which indicates the equilibrium status of the system [10–11]. All results of the MD simulations in this study were obtained under system equilibrium conditions to ensure the accuracy of the results. Figure S1 shows the temperature and energy distribution during the final NPT-MD simulations of the layer-structured composites.

3 Cohesive energy density and solubility parameter

The solubility parameters of polymers are important parameters to estimate the miscibility between polymers [12]. According to Eq. (S1), the solubility parameter (δ) is defined as the root of the cohesive energy density (CED, D_c):

$$\delta = \sqrt{D_c} \tag{S1}$$

CED describes the strength of the interaction between molecules of a material, which is defined according to Eq. (S2) as the ratio between the cohesive energy (E_{coh}) and the volume (V):

$$\mathrm{CED} = \frac{E_{coh}}{V} \tag{S2}$$

The values of δ and CED of PVDF and LDPE were calculated by MD simulations shown in Table S3 [13–14]. As shown, the calculated values of δ and CED are in good agreement with the experimental values, indicating the feasibility of the model and the accuracy of the MD simulations. Meanwhile, the δ values of PVDF and LDPE vary wildly, reflecting the poor miscibility between PVDF and LDPE.

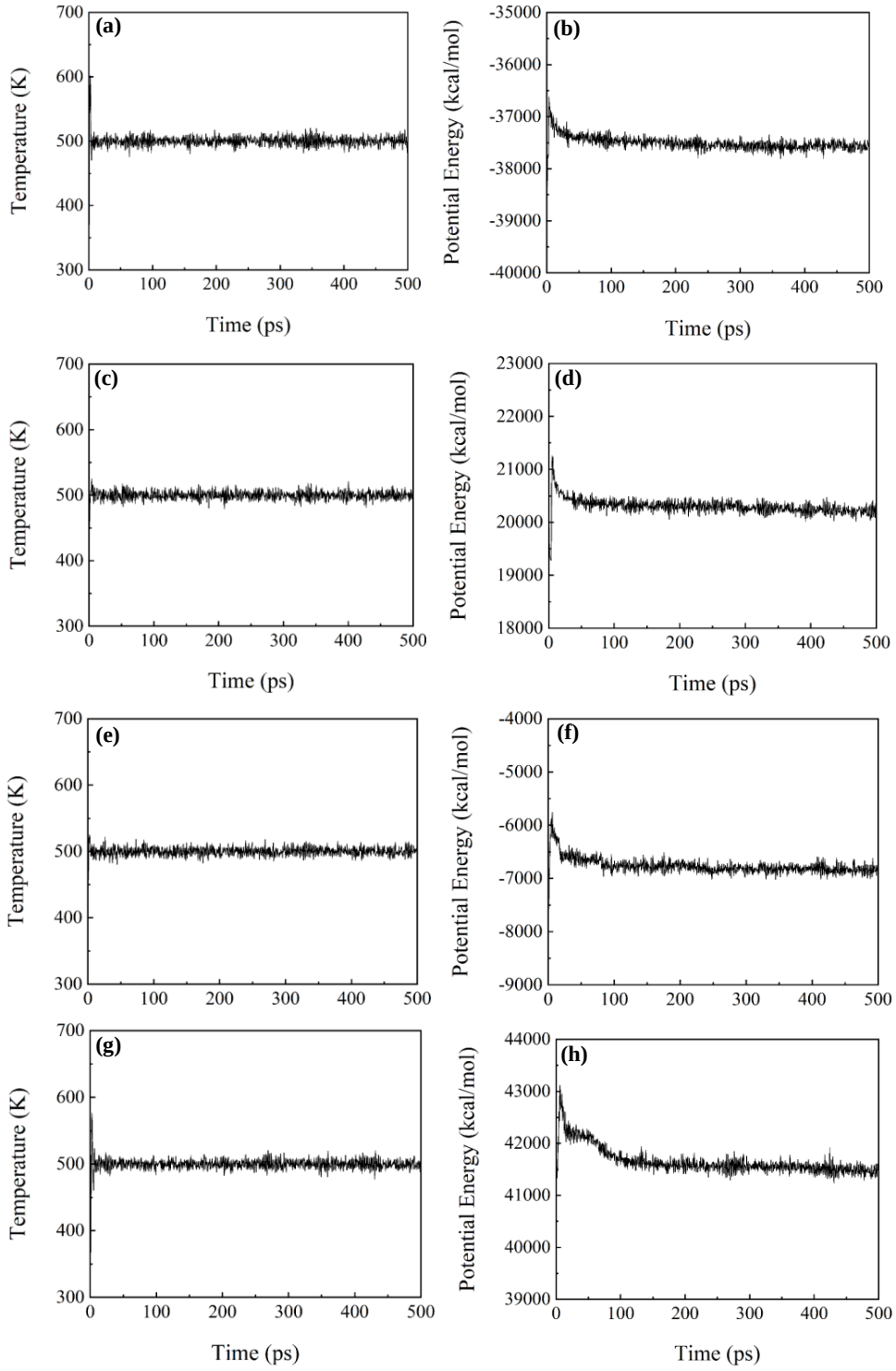

Fig. S1 Temperature and energy distribution curves during the final NPT-MD simulations of the composites of **(a)(b)** PVDF–LDPE, **(c)(d)** PVDF–BT20/LDPE, **(e)(f)** BT20/PVDF–LDPE, and **(g)(h)** BT20/PVDF–BT20/LDPE.

Table S3 The calculated and experimental values of δ and CED of LDPE and PVDF

Sample	Calculated value		Experimental value [13–14]	
	$CED_{MD}/(J\cdot m^{-3})$	$\delta_{MD}/(J\cdot cm^{-3})^{0.5}$	$CED_{exp}/(J\cdot m^{-3})$	$\delta_{exp}/(J\cdot cm^{-3})^{0.5}$
LDPE	3.060×10^{8}	17.488	2.916×10^{8}	17.076
PVDF	4.991×10^{8}	22.342	5.382×10^{8}	23.200

4 Binding energy

The binding energy is an important parameter reflecting the interface interaction between layers and the stability of the interface. The binding energy of the interlayer interface can be calculated according to Eq. (S3) [15–16]. In Eq. (S3), E_{bind} is the binding energy, $E_{interaction}$ is the interaction energy, E_{total} is the total energy of the layer structure system, E_{layer1} is the first layer energy, and E_{layer2} is the second layer energy.

$$E_{bind} = -E_{interaction} = -[E_{total} - (E_{layer1} + E_{layer2})] \quad (S3)$$

As shown in Tables S4 and S5, the binding energy shows higher value under 1 GPa@500 K than that under 0.0001 GPa@298 K, which indicates that there is a certain interaction between the layers to form a relatively stable system at high temperature and high pressure. The binding energies of PVDF–BT20/LDPE and BT20/PVDF–BT20/LDPE under 1 GPa@500 K are larger than those of PVDF–LDPE and BT20/PVDF–LDPE.

Table S4 The binding energy ($kcal\cdot mol^{-1}$) between the layers of PVDF–LDPE, BT20/PVDF–LDPE, PVDF–BT20/LDPE, and BT20/PVDF–BT20/LDPE under the conditions of 298 K and 0.0001 GPa

Sample	E_{total}	E_{layer1}	E_{layer2}	$E_{interaction}$	E_{bind}
PVDF–LDPE	−39705	−41267	1844	−282	282
BT20/PVDF–LDPE	−9439	−11084	1922	−277	277
PVDF–BT20/LDPE	17812	−41082	59464	−570	570
BT20/PVDF–BT20/LDPE	38762	−19604	58570	−204	204

Table S5 The binding energy ($kcal\cdot mol^{-1}$) between the layers of PVDF–LDPE, BT20/PVDF–LDPE, PVDF–BT20/LDPE, and BT20/PVDF–BT20/LDPE under the conditions of 500 K and 1 GPa

Sample	E_{total}	E_{layer1}	E_{layer2}	$E_{interaction}$	E_{bind}
PVDF–LDPE	−37546	−40275	3094	−365	365
BT20/PVDF–LDPE	−6778	−9451	3000	−327	327
PVDF–BT20/LDPE	20295	−39847	61094	−952	952
BT20/PVDF–BT20/LDPE	41559	−17695	60116	−862	862

5 Metallographic photographs

Figure S2 shows a cross-sectional metallographic photograph of the composite at 100× magnification. As shown in Fig. S2, there are no gaps and cracks between the layers. The two layers are relatively closely combined.

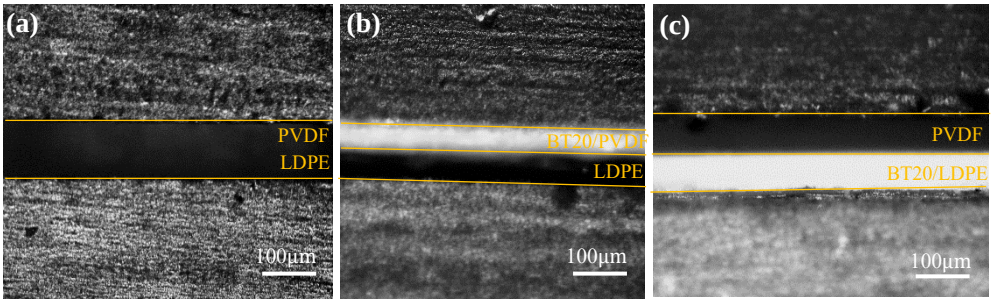

Fig. S2 The metallographic microscope photos of **(a)** PVDF–LDPE, **(b)** BT20/PVDF–LDPE, and **(c)** PVDF–BT20/LDPE at 100× magnification.

6 Characteristic breakdown strengths

The Weibull cumulative probability function was employed to analyze the characteristic breakdown strength of composites, as shown in following Eq. (S4) [17]:

$$P(E) = 1 - \exp\left[-\left(\frac{E}{E_\mathrm{b}}\right)^{\beta}\right] \tag{S4}$$

Taking logarithms on both sides of Eq. (S4), linear Eq. (S5) can be obtained as follows:

$$\ln\{-\ln[1-P(E)]\} = \beta(\ln E - \ln E_\mathrm{b}) \tag{S5}$$

where, $P(E)$ is the cumulative probability of electric failure, E is the experimental breakdown strength, E_b is the characteristic breakdown strength referring to the breakdown strength at the cumulative failure probability of 63.2%, and β is the shape parameter associated with the linear regressive fitting of the distribution [18]. Table S6 shows the shape parameters and characteristic breakdown strengths of the composites.

Table S6 Shape parameters and characteristic breakdown strengths

Sample	Shape parameter (β)	Characteristic breakdown strength/(kV·mm^{-1})
PVDF	12.84	193.4
LDPE	15.34	222.5
PVDF–LDPE	10.39	237.8
BT20/PVDF	8.11	97.6
BT20/LDPE	9.17	109.7
PVDF–BT20/LDPE	9.15	188.9
BT20/PVDF–LDPE	8.09	164.8
BT20/PVDF–BT20/LDPE	5.66	117.5

7 Energy storage performances

Figure S3 shows *P*–*E* loops of the composites. The energy density (U) of the composites is obtained from Eq. (S6) [19], and the charge–discharge efficiency (η) is obtained from Eq. (S7) [20]:

$$U = \int_{P_\mathrm{o}}^{P_\mathrm{max}} E \,\mathrm{d}\, P \tag{S6}$$

$$\eta/\% = \frac{U_d}{U_c} \times 100 \tag{S7}$$

where E is the electric field, P is the polarization, and P_{max} is the maximum polarization intensity under the maximum electric field. When $P_o = 0$, U is the charge energy density (U_c); when $P_o = P_r$ (remnant polarization), U is the discharge energy density (U_d).

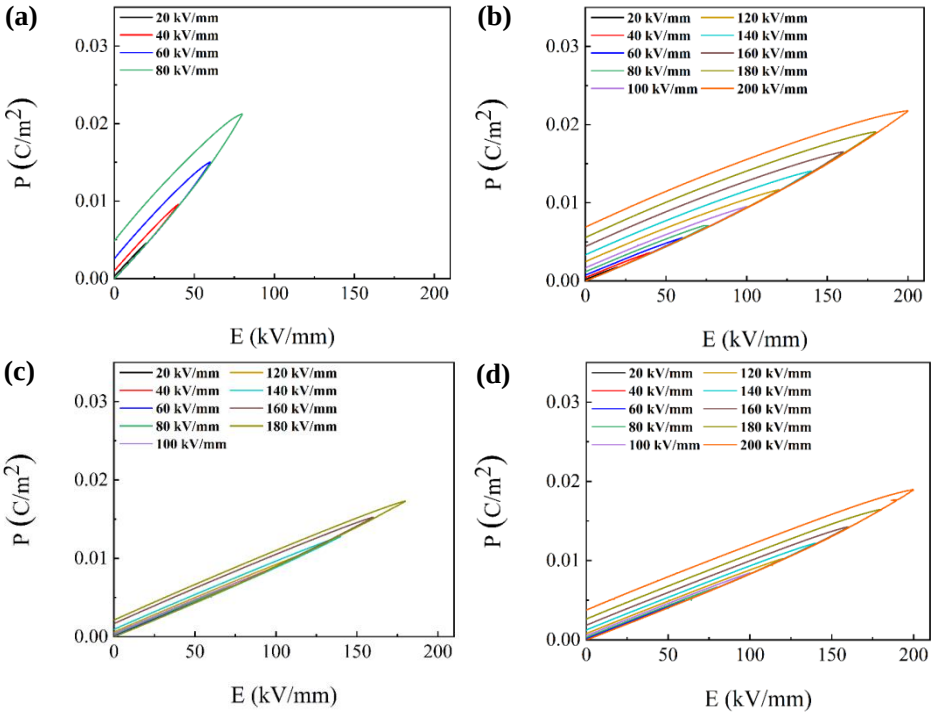

Fig. S3 *P–E* loops of the composites of **(a)** BT20/PVDF, **(b)** PVDF, **(c)** BT20/PVDF–LDPE, and **(d)** PVDF–BT20/LDPE under different electric fields.

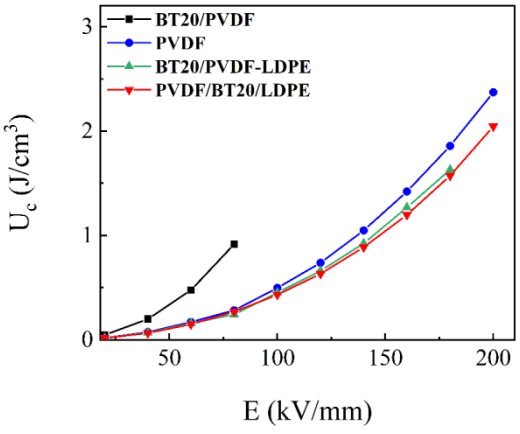

Fig. S4 Variations of U_c with the electric field for different samples.

According to Eqs. (S6) and (S7), it is seen that the wider the *P–E* loop, the more energy loss of the composites and the lower η. The BT20/PVDF and PVDF composites exhibit wider loops than the layer-structured composites under the same external electric field, indicating enhanced energy loss and reduced charge–discharge efficiency.

Figure S4 shows U_c values of the composites. According to Eq. (S6), U_c increases with the enhancement of P_{max} under the same electric field. As the electric field increases, P_{max} increases and U_c also increases. Therefore, as is shown in Fig. S4, the U_c value of PVDF is larger than that of the layer-structured composites.

8 Distribution of electric field

The double-layer structured film is equivalent to the series connection of two capacitors with different permittivity and breakdown strength. For the convenience of expression, the layer with a high dielectric permittivity is called a dielectric layer, and the layer with a low dielectric permittivity is called an insulating layer. The electric field distribution of the layer-structured composites can be calculated by following equations [21–22] according to the series capacitor model (SCM):

$$E_1 = \frac{U}{d_1 + \frac{\varepsilon_1}{\varepsilon_2} \cdot d_2} \tag{S8}$$

$$E_2 = \frac{U}{d_2 + \frac{\varepsilon_2}{\varepsilon_1} \cdot d_1} \tag{S9}$$

where, E_1 and E_2 are electric field strengths of the dielectric layer and the insulating layer, respectively; U is the applied test voltage; d_1 and d_2 are thicknesses of the dielectric layer and the insulating layer, respectively; ε_1 and ε_2 are dielectric permittivity values of the dielectric layer and the insulating layer at 10^2 Hz, respectively.

The electric field strength of each layer of the layer-structured composites is calculated according to Eqs. (S8) and (S9), and the relevant parameters of the four groups of layer-structured films are shown in Table S7. It shows that the electric field strength of the layer-structured film is redistributed among the layers under the applied electric field [23–24]. The electric field strength of the dielectric layer is obviously lower than that of the insulating layer while the breakdown field strengths of the four groups of the layer-structured films are lower than the electric field strength of the insulating layer, but higher than that of the dielectric layer. For example, the electric field strength of the LDPE layer of BT20/PVDF–LDPE is 267.3 kV·mm^{-1}, which exceeds the breakdown field strength of LDPE (222.5 kV·mm^{-1}).

Table S7 Electric field strength and related parameters of each layer in the layer-structured film

Sample	Layer	d/μm	ε	E/(kV·mm^{-1})	U/kV	E_2/E_1
PVDF–LDPE	PVDF	50	9.20	100.8	22.87	3.54
	LDPE	50	2.60	356.6		
BT20/PVDF–BT20/LDPE	BT20/PVDF	50	20.11	47.7	10.69	3.49
	BT20/LDPE	50	5.77	166.3		
BT20/PVDF–LDPE	BT20/PVDF	50	20.11	34.6	15.09	7.73
	LDPE	50	2.60	267.3		
PVDF–BT20/LDPE	PVDF	50	9.20	129.9	16.85	1.59
	BT20/LDPE	50	5.77	207.0		

9 Results of finite element analysis

Figures S5 and S6 show surface electric field distributions and surface charge energy density distributions of the composites, respectively.

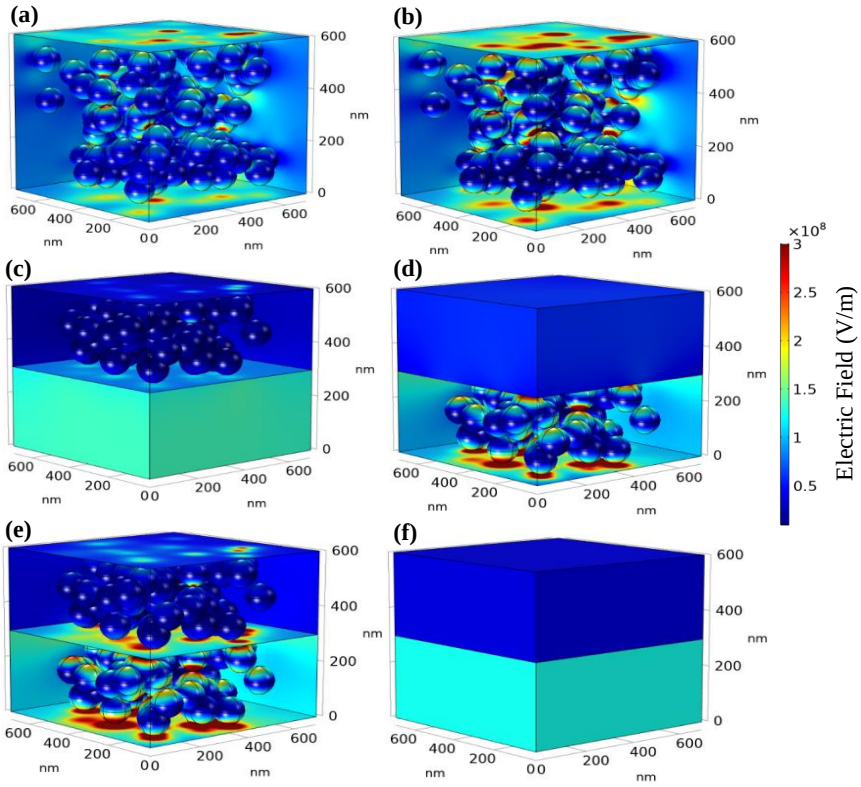

Fig. S5 Surface electric field distributions of **(a)** BT20/PVDF, **(b)** BT20/LDPE, **(c)** BT20/PVDF–LDPE, **(d)** PVDF–BT20/LDPE, **(e)** BT20/PVDF–BT20/LDPE, and **(f)** PVDF–LDPE.

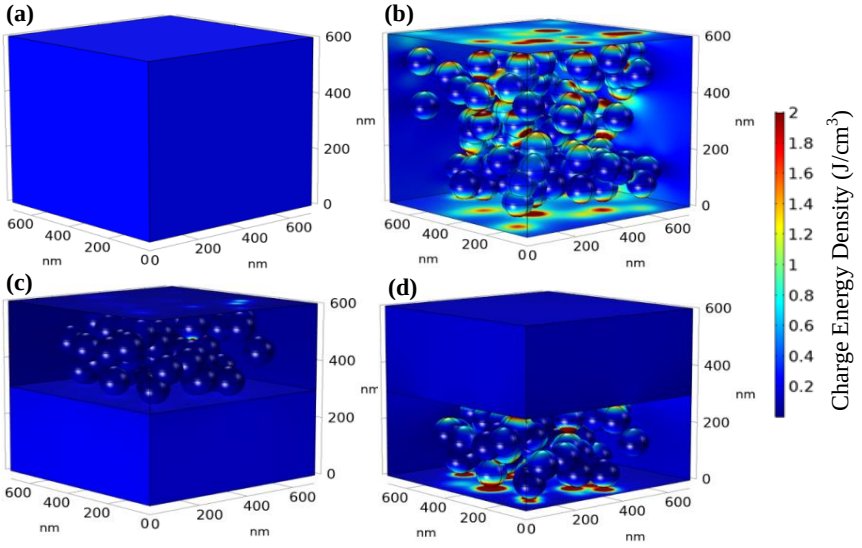

Fig. S6 Surface charge energy density distributions of **(a)** PVDF, **(b)** BT20/PVDF, **(c)** BT20/PVDF–LDPE, and **(d)** PVDF–BT20/LDPE.

Table S8 gives the E_2/E_1 calculated by FEA simulation of the electric field distribution of the layer-structured composites. Table S9 gives the simulated charge energy density by FEA. The electric field strengths of the dielectric layer and the insulating layer (E_2/E_1) by FEA in Table S8 are close to the E_2/E_1 results by SCM in Table S7, indicating the rationality of FEA.

Table S8 Electric field intensity of each layer in the layer-structured composites by FEA

Sample	Layer	Coordinate	$E/(\mathrm{V\cdot m^{-1}})$	E_2/E_1
PVDF–LDPE	PVDF	(−300, −170)	3.5254×10^7	3.54
	LDPE	(−300, −430)	1.2475×10^8	
BT20/PVDF–BT20/LDPE	BT20/PVDF	(−300, −170)	3.1387×10^7	3.13
	BT20/LDPE	(−300, −430)	9.8304×10^7	
BT20/PVDF–LDPE	BT20/PVDF	(−300, −170)	1.9509×10^7	6.95
	LDPE	(−300, −430)	1.3553×10^8	
PVDF–BT20/LDPE	PVDF	(−300, −170)	5.5077×10^7	1.56
	BT20/LDPE	(−300, −430)	8.5862×10^7	

As shown in Table S9, when the electric field is 80 $\mathrm{kV\cdot mm^{-1}}$, the U_c experimental value of PVDF is 0.28 $\mathrm{J\cdot m^{-3}}$, and the FEA simulation value is 0.26 $\mathrm{J\cdot m^{-3}}$. The U_c experimental value of BT20/PVDF is 0.92 $\mathrm{J\cdot m^{-3}}$, and the FEA simulation value is 0.89 $\mathrm{J\cdot m^{-3}}$. The FEA simulated U_c value is close to the U_c experimental value, indicating the rationality of FEA.

Table S9 Charge energy density and related parameters of the composites by FEA

Sample	Layer	Coordinate	$U_c/(\mathrm{J\cdot cm^{-3}})$
PVDF	PVDF	(−165, −375)	0.26
BT20/PVDF	BT20/PVDF	(−165, −375)	0.89
BT20/PVDF–LDPE	BT20/PVDF	(−300, −170)	0.02
	LDPE	(−300, −430)	0.21
PVDF–BT20/LDPE	PVDF	(−300, −170)	0.12
	BT20/LDPE	(−300, −430)	0.16

References

[1] Wang Y F, Cui J, Yuan Q B, et al. Significantly enhanced breakdown strength and energy density in sandwich-structured barium titanate/poly(vinylidene fluoride) nanocomposites. Advanced Materials, 2015, 27(42): 6658–6663

[2] Nosé S. Constant temperature molecular dynamics methods. Progress of Theoretical Physics Supplement, 1991, 103: 1–46

[3] Berendsen H J C, Postma J P M, van Gunsteren W F, et al. Molecular dynamics with coupling to an external bath. The Journal of Chemical Physics, 1984, 81: 3684–3690

[4] Rappé A K, Casewit C J, Colwell K S, et al. A full periodic table force field for molecular mechanics and molecular dynamics simulations. Journal of the American Chemical Society, 1992, 114: 10024–10035

[5] Casewit C J, Colwell K S, Rappé A K. Application of a universal force field to organic molecules. Journal of the American Chemical Society, 1992, 114: 10035–10046

[6] Hofmann D, Fritz L, Ulbrich J, et al. Detailed-atomistic molecular modelling of small molecule diffusion and solution processes in polymeric membrane materials. Macromolecular Theory and Simulations, 2000, 9(6): 293–327

[7] Wei Q H, Wang Y N, Chai W H, et al. Effects of composition ratio on the properties of poly(vinyl alcohol)/poly (acrylic acid) blend membrane: a molecular dynamics simulation study. Materials & Design, 2016, 89: 848–855

[8] Bhowmik R, Katti K S, Katti D. Molecular dynamics simulation of hydroxyapatite–polyacrylic acid interfaces. Polymer, 2007, 48(2): 664–674

[9] Zhang S G, Wang F Y, Tan X Y. Molecular dynamics simulation the hydroxyapatite scale inhibition mechanism of water-soluble polymers. Journal of Theoretical and Computational Chemistry, 2010, 9(5): 889–902

[10] Tong Z F, Xie Y B, Zhang Y H. Molecular dynamics simulation on the interaction between polymer inhibitors and β-dicalcium silicate surface. Journal of Molecular Liquids, 2018, 259: 65–75

[11] Wang Y, Wei Q, Pan F, et al. Molecular dynamics simulations for the examination of mechanical properties of hydroxyapatite/poly α-n-butyl cyanoacrylate under additive manufacturing. Bio-Medical Materials and Engineering, 2014, 24: 825–833

[12] Jawalkar S S, Adoor S G, Sairam M, et al. Molecular modeling on the binary blend compatibility of poly (vinyl alcohol) and poly (methyl methacrylate): an atomistic simulation and thermodynamic approach. The Journal of Physical Chemistry B, 2005, 109(32): 15611–15620

[13] Meng F, Liu D, Wang Y, et al. High polymer modified asphalt comprises styrene-butadiene block polymer which is star-shaped material with specific particle size, low density polyethylene with specific solubility parameter and matrix asphalt. CN112724697-A, CN112724697-B, 2021-07-30

[14] Bottino A, Capannelli G, Munari S, et al. Solubility parameters of poly(vinylidene fluoride). Journal of Polymer Science Part B: Polymer Physics, 1988, 26(4): 785–794

[15] Zeng J P, Zhang S G, Gong X D, et al. Molecular dynamics simulation of interaction between calcite crystal and phosphonic acid molecules. Chinese Journal of Chemistry, 2010, 28(3): 337–343

[16] Zeng J P, Wang F H, Zhou C, et al. Molecular dynamics simulation on scale inhibition mechanism of polyepoxysuccinic acid to calcium sulphate. Chinese Journal of Chemical Physics, 2012, 25(2): 219–225

[17] Wang L, Luo H, Zhou X F, et al. Sandwich-structured all-organic composites with high breakdown strength and high dielectric constant for film capacitor. Composites Part A: Applied Science and Manufacturing, 2019, 117: 369–376

[18] Pan Z, Yao L, Zhai J, et al. Excellent energy density of polymer nanocomposites containing $BaTiO_3$@Al_2O_3 nanofibers induced by moderate interfacial area. Journal of Materials Chemistry A, 2016, 4(34): 13259–13264

[19] Pu L Y, Tang J Y, Gu X C, et al. Dielectric and energy storage properties of nanocomposites with core–shell paraffin-engineered $BaTiO_3$ in polyimides. Journal of Materials Science: Materials in Electronics, 2021, 32(5): 5886–5897

[20] Xie Y C, Wang J, Yu Y Y, et al. Enhancing breakdown strength and energy storage performance of PVDF-based nanocomposites by adding exfoliated boron nitride. Applied Surface Science, 2018, 440: 1150–1158

[21] Zhang Y, Chi Q G, Liu L Z, et al. Enhanced electric polarization and breakdown strength in the all-organic sandwich-structured poly(vinylidene fluoride)-based dielectric film for high energy density capacitor. APL Materials, 2017, 5(7): 076109

[22] Shen Y, Shen D S, Zhang X, et al. High energy density of polymer nanocomposites at a low electric field induced by modulation of their topological structure. Journal of Materials Chemistry A, 2016, 4(21): 8359–8365

[23] Li Q, Liu F H, Yang T N, et al. Sandwich-structured polymer nanocomposites with high energy density and great charge–discharge efficiency at elevated temperatures. Proceedings of the National Academy of Sciences of the United States of America, 2016, 113: 9995–10000

[24] Xie B, Zhang Q, Zhang L, et al. Ultrahigh discharged energy density in polymer nanocomposites by designing linear/ferroelectric bilayer heterostructure. Nano Energy, 2018, 54: 437–446